Ocean Sci. Discuss., 11, 1473–1517, 2014
www.ocean-sci-discuss.net/11/1473/2014/
doi:10.5194/osd-11-1473-2014

Ocean Science
Discussions
Open Access

Detailed temperature–salinity distribution in the Northeast Atlantic from ship and Argo vertical casts

I. Bashmachnikov[1,2], F. Neves[1], A. Nascimento[1], J. Medeiros[1], I. Ambar[1,2], J. Dias[1,2], and X. Carton[3]

[1]Centro de Oceanografia da Faculdade de Ciências, Universidade de Lisboa, (CO-FCUL), Campo Grande, 1749-016, Lisbon, Portugal
[2]Departamento de Engenharia Geográfica, Geofísica e Energia (DEGGE), Faculdade de Ciências, Universidade de Lisboa, Campo Grande, 1749-016 Lisboa, Portugal
[3]Laboratoire de Physique des Océans, UMR 6523, Université de Bretagne Occidentale, 6 avenue Le Gorgeu, 29200 Brest, France

Received: 15 April 2014 – Accepted: 21 May 2014 – Published: 11 June 2014

Correspondence to: I. Bashmachnikov (igorb@fc.ul.pt)

Published by Copernicus Publications on behalf of the European Geosciences Union.

Abstract

The present study defines new interpolation functions for hydrological data. These functions are applied to generate climatological maps of temperature–salinity distribution with 25 m depth interval and 30 km space interval (MEDTRANS data-set). The data underwent a rigorous data quality control, having passed several filtering procedures. The gridding was done on neutral density surfaces, which allows better representation of the relative intensity of thermohaline fronts for the same gridding radius. The gridding was done using multi-pass Barnes' Optimum Interpolation procedure with spatially variable size of the gridding window. The shape of the window accounted for topographic influence: the dominant along-slope direction of water mass transport. One of the new features was the use of a local ratio of topographic to planetary β-effects to define the shape of the window as a function of the relative importance of the topographic influence. The N/f ratio was used for simulation of the baroclinic decrease of the topographic influence on water mass transport with the distance from the bottom. The gridded fields are available at the web-site of the Center of Oceanography of the University of Lisbon (http://co.fc.ul.pt/en/data).

The new MEDTRANS climatology gives more details to the distribution of water characteristics in the Subtropical Northeast Atlantic, in particular near the Iberian Peninsula. The geostrophic currents relative to the 1900 m reference level demonstrate the local circulation features, in good correspondence to the theory and to previous studies: the acceleration in the meanders of the Azores current; the cyclonic gyre in the Gulf of Cadiz; the splitting and separation of the Mediterranean Water outflow from the continental slope near the Gorringe and the Galicia banks. Those features are not reproduced by the alternative climatologies.

Seasonal climatologies, computed for the warm (May–October) and cold (November–April) seasons, revealed stronger zonal extension of the upper ocean patterns during the warm season, as compared to the cold one. At the Iberian continental

OSD
11, 1473–1517, 2014

slope, the seasonality manifested itself in more saline and denser lower core of the Mediterranean Water during the warm season as compared to the cold season.

1 Introduction

This work presents detailed maps of climatic temperature–salinity distribution of ocean characteristics in the Subtropical Northeast Atlantic (25–45° N and 6–35° W), with special focus on the propagation of the Mediterranean Water (MW) in Atlantic. This study was felt necessary since the existing global climatic fields (WOA09, WOA13, Schmidtko et al., 2013; Troupin et al., 2010) do not provide sufficiently detailed or noise-free mapping of the temperature–salinity variations at the intermediate water level near the Iberian Peninsula where the spreading of Mediterranean Water is characterized by rather high temperature–salinity gradients. The sufficiently large quantity of data and their even spatial distribution in the study region allow us to base the parameters of the gridding procedure on characteristics of the local hydrodynamics. This increases the reliability of the derived fields of regional circulation patterns.

The study region is dominated by two nearly zonal flows: the southern branch of the North Atlantic Current (SNAC) that crosses the Mid-Atlantic Ridge (MAR) at 45–48° N (Bower et al., 2002), and the Azores Current (AzC), which crosses the MAR at 34–35° N (Klein and Siedler, 1989). The SNAC separates subtropical waters from colder and fresher subpolar waters while the 60 km wide jet-like AzC separates warm and salty tropical waters from the subtropical waters. The associated Azores front is attributed to a zone of enhanced Ekman transport convergence (Käse and Siedler, 1982) as well as to the formation of a beta-plume due to the MW outflow from the Strait of Gibraltar (Jia, 2000; Volkov and Fu, 2010). A weak (2 cm s^{-1}) and narrow westward subsurface flow, the Azores Counter Current (AzCC), is positioned immediately to the north of the AzC (Onken, 1993). Several works address the dominance of the eastward mean drift in the upper 200–300 m layer over all the Azores region, then turning south

OSD
11, 1473–1517, 2014

(Pollard and Pu, 1985). More recent studies suggest that the flux is separated in several weak meandering southeastwards jets (Paillet and Mercier, 1997).

Near the Iberian and northwest African coasts, Portugal (PC) and Canary (CC) currents represent a system of wide shallow flows and coastally trapped surface upwelling jets (Martins et al., 2002; Perez et al., 2001; Pelegri et al., 2005; Nolasco et al., 2013). Below the CC a deeper northward flow, trapped by the African continental slope, transports the Antarctic Intermediate Water (AAIW) as far as the Gulf of Cadiz (Louarn and Morin, 2011). Underneath the PC, the deep poleward flow incorporates the Mediterranean Undercurrent (MUC), which is separated in: (i) two classical cores, the generally recognized upper and lower cores; (ii) the shallow core, identified in the early eighties (e.g. Ambar, 1983); and (iii) the recently discovered deep core, below the classical cores (e.g. Ambar et al., 2008).

The eddy activity in the region is mostly the result of instability of the baroclinic currents. The AzC forms anticyclonic meanders which are transformed into dominating anticyclonic structures to the north of the AzC (Pollard and Pu, 1985; Alves and Verdière, 1999). The meanders have typical wavelengths of 300–400 km and move westwards at the speed of about 1.8 cm s^{-1} (Pingree, 2002). The anticyclonic eddies, having detached from the AzC, have a radius of the order of 100 km. The mean transport by the anticyclones formed to the north of the AzC was suggested to constitute the westward flow named the AzCC (Alves and Verdière, 1999).

The frontal zones in the region are relatively narrow, but the meandering together with the seasonal and interannual variations of the current position should enlarge the width of the currents in the mean climatic fields.

There are several global and regional data bases covering the study region. The most known world data base, the World Ocean Atlas 2009 (WOA09), has a minimum radius of the gridding window of 444 km and a grid resolution of $1^{\circ} \times 1^{\circ}$. During this work, the new version of the World Ocean Atlas 2013 (WOA13) was published. The WOA13 has a radius of the gridding window of 214–321 km and a maximum grid resolution of $0.25^{\circ} \times 0.25^{\circ}$, and it showed a significantly improved climatology in the study

OSD
11, 1473–1517, 2014

region, as compared to WOA09. At the same time, the gridding procedure with radius of influence of more than 200 km significantly oversmoothes the details of the flows_especially at the Iberian continental slope. In particular, the MUC of 20–80 km width cannot be adequately reproduced in WOA13 (details are given in the Sect. 3). In this study the bottom trapped MUC signature is better reproduced due to the reduction of the local radius of influence to 70 km near the Iberian slope. The gridding window, extended along steep topographic slopes, as well as the use of isopycnic mapping, give additional advantages in enlightening the details of this climatology, compared to the isobaric mapping used in WOA. In particular, for the same radius of influence, the isobaric approach is known to have stronger artificial reduction of intensity of fronts as compared to the isopycnic one. Isobaric mapping may also produce artificial temperature–salinity anomalies near frontal zones, this not happening for isopycnic gridding procedure (Lozier et al., 1994).

In the present climatology the radius of influence of the gridding function could be reduced due to rigorous initial data control and the developed methodology of eddy filtering on neutral density surfaces. This is described in the Sect. 2.

Among other climatologies covering the study region, we compare our data with AMA (Roemmich and Gilson, 2009), MIMOC (Schmidtko et al., 2013) and DIVA (Troupin et al., 2010). AMA climatology is based exclusively on ARGO data. The data-set does not allow mapping the MUC along the continental slope of the Iberian Peninsula (very few ARGO floats there). Therefore, it will not be used for comparison. DIVA climatology has too much noise for climatic fields and it also will not be used for comparison. The MIMOC climatology has $0.5^{\circ} \times 0.5^{\circ}$ resolution and is also based on isopycnic mapping. We will show below that our results closely correspond to the results of MIMOC in the upper ocean. At the same time, MIMOC has the disadvantage of lower resolution and the use of sigma surfaces instead of neutral density surfaces used in this paper. MIMOC also produces artifacts in the temperature–salinity distribution below 1500 m (see Sect. 3).

OSD
11, 1473–1517, 2014

Neutral density surfaces (McDougall, 1987) are a generalisation of the concept of standard σ_n ($n = 0$, 1, 2, etc.) surfaces. The former are parallel to the latter at their reference level. Along a neutral density surface, salinity variations are compensated by those of temperature: $\alpha \nabla_n \theta - \beta \nabla_n S = 0$, where α is the thermal expansion coefficient and β is the saline contraction coefficient and the gradients (both are temperature–salinity–pressure-dependent), the gradient ∇_n are taken along the neutral density surface. Therefore, a particle travelling along a neutral density surface does not experience the effect of the buoyancy force. This is not true for a particle travelling along σ_n surfaces (McDougall, 1987).

The present study uses the National Oceanographic Data Center (NODC) data-set, which includes all available vertical temperature–salinity profiles (CTD, ARGO, XCTD, etc.) to produce the high resolution maps on Mercator projection used by AVISO altimetry (AVISO). In the study region, the grid has 0.33° resolution in latitude and variable resolution in longitude (around 0.30°). An advantage of this gridding procedure is that it allows straightforward comparison or merging of the dynamic depths obtained from in-situ data with the free-surface topography available from satellites. The present climatology was obtained in the framework of the project MEDTRANS, and will further be referred as MEDTRANS climatology.

2 Materials and methods

Data from the World Ocean Database (WOD) were downloaded from the National Oceanographic Data Center (NODC, http://www.nodc.noaa.gov/): CTD (Conductivity–Temperature–Depth, high vertical resolution of typically 1 m or less) and PFL (Profiling Float, medium vertical resolution of typically 1–10 m, mainly obtained from ARGO profiling float array), OSD (Ocean Station Data, low vertical resolution of typically more than 10 m).

Within the study region, there were over 54 000 profiles (Table 1). The spatial distribution density of CTD (and to less extent the OSD) profiles showed a tendency to

OSD
11, 1473–1517, 2014

decrease from the continental margin seawards, while the PFL profiles covered the region rather uniformly, but only the areas with water depth exceeding 1000 m.

A quality control procedure was applied to all NODC data, attributing different flags to the data-points according to their quality. The first step consists in comparing the observed vertical profiles with the corresponding climatological temperature and salinity profiles in each of the $1^\circ \times 1^\circ$ squares obtained from WOA09, interpolated to the profiles' positions. A part of a profile is considered to be bad if it exhibits a strong spike, leading to a density inversion, or if the whole profile deviates from the climatological mean profile for more than 5 standard-deviations. For the upper 100 m layer and the MW layer, the criterion was not used since the extreme natural deflections in those layers exceed the 5 standard-deviations relative to the smoothed WOA09 fields.

The next step consists in testing the profiles for static stability. In the parts of the profiles where a density inversion existed and exceeded 0.02 kg m^{-3} over less than 200 m depth range, the attempt to correct the inversion by removing spikes in temperature or salinity was made. For all cases we tended to correct first the salinity spikes, since salinity is in general more vulnerable to observational errors, and then, if necessary, the temperature spikes. Finally, the profiles were additionally eye-checked to make an expert decision on acceptance or removal of the profiles previously marked as "dubious" and to detect the occurrences of possible algorithm failures. The portions of the profiles treated as "bad" were blanked. If data gaps existed only in the temperature or in the salinity profile, and their size did not exceeded 200 m, the gaps were linearly (low resolution OSD) or polynomially (CTD and PFL) interpolated to the corresponding z-levels. The resulting profiles were reduced to a standard vertical resolution of 25 m.

The results showed that 94 % of the profiles contained at least 50 % of good values for both temperature and salinity (Table 1). Distributions of the salinity data-points that passed the filtering procedure at the selected depth levels are presented in Fig. 1a–c. In the upper 1900 m layer, the data are rather uniformly distributed (Fig. 1a and b), while below 2000 m, the existence of solely CTD/OSD casts results in large spatial data gaps in some areas (Fig. 1c). Figure 1d shows the vertical profile of the amount of

OSD
11, 1473–1517, 2014

valid data in the study region. A maximum at 100 m and a rapid decrease below 1900 m are noted. Observations at the standard oceanographic levels (OSD data) formed the "spikes" of higher data concentration in the panel. Except for the slightly larger amount of data, the temperature data-points distribution is similar to that of salinity, presented in Fig. 1.

Mediterranean Water eddies (meddies) exhibit themselves as the most pronounced temperature–salinity anomalies in the MW layer. They are not filtered at the previous steps since they do not cause density inversions, but their presence adds strong additional noise to the climatic fields. The casts across the meddies were detected using Richardson's criterion (Richardson et al., 1991) and were eliminated, together with the surrounding profiles within 50 km spatial and 30 day time ranges, which may be influenced by the meddy cores. The area of the Mediterranean Undercurrent, the slope of Iberian Peninsula with water depths less than 2500 m, was excluded from this latter filtration.

Further experiments show that OSD profiles along some of XCTD routes evidence a consistent rise of temperature and salinity relative to WOA09 climatic profiles, especially noticeable below the 1500 m level. This was not observed for the CTD or PFL profiles and was presumably due to incorrect estimation of the instrument depth for XCTD instruments (Levitus et al., 2008). To eliminate the effect, the sum of temperature and salinity deviations of the OSD profiles from WOA09 between 1500 and 2000 m were computed. In case of a random error, these sums should be close to zero, otherwise the affected profiles underwent an iterative filtering procedure.

In addition, consecutive profiles of the same PFLs were removed when a degradation of the salinity sensor with time was noted.

Further gridding was done on neutral density surfaces (McDougall, 1987). First, a value of neutral density was attributed to each level of the individual profiles (Jackett and McDougall, 1997). Then, pressure, temperature and salinity distributions were obtained for the following 53 neutral density surfaces (G). The G-surfaces were selected

OSD
11, 1473–1517, 2014

to be rather uniformly distributed in depth, keeping the mean distance between the surfaces less than 50 m in the upper 1500 m layer, and less than 100 m below.

After calculation of the neutral density surfaces, an additional filter was applied to remove remnant instrumental errors and eddy noise. Both eddies and currents deflect the isopycnals from the climatic state. Rotation velocities in eddies are higher than advection velocities in mean currents, therefore, even if the length scales of both dynamic structures are the same, eddies generally deflect isopycnic surfaces more strongly than the mean currents. This difference can be used to design a filter. The parameters are chosen to limit the vertical velocity variation (d_zV) across the interface of the G-surface: $\frac{d_zV}{\Delta z} = \frac{N^2}{f}\frac{\partial G}{\partial l}$. Taking $N^2 = 5\times10^{-5}\,\mathrm{s}^{-1}$ and $\frac{\partial G}{\partial l}$ being less than 200 m per 200 km, we get that d_zV should be less than $5\,\mathrm{cm\,s}^{-1}$ per $\Delta z = 100$ m. In the Azores Current the gradient is less than $3\,\mathrm{cm\,s}^{-1}$ per 100 m (Comas-Rodriguez et al., 2011). About 100 km downstream from the Strait of Gibraltar, the velocity vertical gradient of the MUC at its upper boundary reach $-30\,\mathrm{cm\,s}^{-1}$ per 100 m (Baringer and Price, 1997), but those vertical gradients are observed only in 10 km distance from the Iberian continental slope. Over the 30 km grid resolution of our study the mean vertical gradients in the MUC drop below $12\,\mathrm{cm\,s}^{-1}$ per 100 m. To account for the higher vertical variations, towards the Iberian Peninsula and in the Gulf of Cadiz the criterion was gradually relaxed to d_zV less than $15\,\mathrm{cm\,s}^{-1}$ per 100 m.

The previous analysis (see also Table 1) gave evidence that CTD and PFL profiles have, in general, higher quality than that of the OSD ones. The latter was a result of generally lower quality of instrumentation used with overall lower vertical resolution. Therefore, in the subsequent gridding procedure the OSD profiles entered with the lower profile weights 1, while CTD/PFL data entered with the profile weights 2.

Following WOA09 methodology we used the Barnes interpolation procedure for obtaining the final maps of water characteristics (Barnes, 1964). Barnes interpolation result (F_{ij}) at the grid point ij was obtained as a weighted sum of the temperature or salinity values C_s of the observational points s, which are inside a certain radius

OSD
11, 1473–1517, 2014

(R). In the original version of the algorithm, the weights $W_{ijs} = e^{-r_{ijs}^2/R^2}$ were Gaussian weight functions of distance r_{ijs} between the grid-point ij and the data-point s, and R is the e-folding scale (85 % of influence of data points at $r \le R$). Then, the initial gridded field was: $F_{ij}^0 = \sum_{s:|s-ij|<R} W_{ijs} C_s / \sum_s W_{ijs}$. Further on, the obtained gridded field was interpolated for the positions of the data grid-points C_s (F_{ijs}^0) and was refined in the iterative procedure $F_{ij}^k = F_{ij}^{k-1} + \sum_{s:|s-ij|<R} W_{ijs} \left(C_s - F_{ijs}^{k-1}\right) / \sum_s W_{ijs}$. This increased the steepness of the interface between the no-pass/pass wavelength domains of the filter, i.e. the sharpness of the resulting frontal zones. For example, the response function of the initial gridded field is $D_0 = e^{-(\pi R/\lambda)^2}$, and the following iterations decrease the range between the fully filtered and fully accepted wavelengths as $D_k = D_0 \sum_{n=1}^{k} (1 - D_0)^{n-1}$ (Barnes, 1964).

A few modifications to the algorithm were made, which are listed below.

Potential vorticity constrains the direction of ocean flows, in particular, by steering them along topography. The inclination of a bottom slope, necessary for effective trapping of the flow, depends on the local ratio of planetary to topographic β-effects. In the absence of friction, the depth-integrated flow is non-divergent (geostrophic) when:

$$V\beta/f - \boldsymbol{v} \cdot \nabla H/H = 0. \quad (1)$$

Here $f = f_0 + \beta y$ is the Coriolis parameter, ∇H is the bottom slope, H is the mean water depth, $\boldsymbol{v}$ is the horizontal velocity vector and V is its meridional component. At the points where the topographic β-effect dominates over the planetary effect, following Schmidtko et al. (2013), we stretched the Gaussian weight function (W_{ijs}) along isobaths. A methodological novelty in this paper is that the algorithm automatically selects the degree to which the topographic β-effect distorts the circular distribution of the isolines of W, using the expression Eq. (1). The resulting weight function is written as

OSD
11, 1473–1517, 2014

follows:

$$W = [wcA_h + (1 - c)]e^{-(r^2/R^2)} \quad (2)$$

The depth dependent function A_h is similar to the one used by Schmidtko et al. (2013): $A_h = \max\left(0.5, \left|1 - 0.5\left|\log\frac{H_{ij}}{H_s}\right|\right|\right)$, but in our gridding procedure, water depth variation between the data point (H_s) and the grid point (H_{ij}) affects the weight function less than in the referred work. The parameter $c = \delta\frac{\nabla H/H}{\beta/f}$ characterizes the relative role of topographic β-effect relative to the planetary β-effect. The possible variations of the parameter are limited to the range from 0 (no influence of bathymetry) to 1 (the maximum influence of bathymetry). The parameter w (see below) accounts for compensation of the decrease of the area of the gridding-window at steep topographic slopes.

Another novelty of the method is that we account for the effect of ocean baroclinicity, i.e. decrease of isopycnal slopes and current intensity with the distance from the sloping bottom. The parameter $\delta = \max\left(0, 1 + \frac{h - H_{ij}}{H_m}\right)$, which is a function of the difference between the gridding level h and the water depth in the grid point (H_{ij}), accounts for the weakening of bottom slope effect on the circulation with the distance from the topography. The maximum distance from the bottom, where the bottom influence becomes insignificant on ocean circulation, can be roughly estimated from the expression $H_m \sim L\frac{f}{N}$ (Ownes and Hogg, 1980). With the ratio $\frac{N}{f} \sim 80$–90, typical for the upper 2000 m layer, and the spatial scale $L \sim 200$ km, which is close to the typical width of the major ocean currents, we get $H_m = 2200$–2500 m. The latter value was used for definition of c in expression Eq. (2).

Care has been taken so that the number of the surrounding points influencing the central grid-point does not have any significant decrease at strongly sloping topography. This decrease results from the narrowing of the window area across isobaths in the areas of very steep bottom slope (continental margins, banks or seamounts); the resulting mean weight over the gridding window may decrease to as much as 30 %, increasing the noise level of the gridded climatology near the topography. This especially

OSD
11, 1473–1517, 2014

strong noise appears in divergence of the computed geostrophic flows. To avoid this effect, the parameter w was introduced in Eq. (2): the ratio of the mean weight in the grid-point to the mean weight when $c = 0$. This results in increase of the weights within the gridding window, not affecting the mean gridding radius.

When friction is taken into account, the right-hand side of Eq. (1) is not zero, but includes the effect of the atmospheric wind torque, bottom frictional torque and the Joint Effect of Baroclinicity and Bottom Relief (JEBAR). The JEBAR is generally small compared to other terms. The bottom frictional torque is efficient only near topography and its effect on the flow results in a gradual change of the depth of the axis or/and of the thickness of a bottom trapped flow. The vorticity pumped into the ocean by the wind torque generates Sverdrup circulation. In the eastern parts of the oceans, the meridional component of the Sverdrup flow is comparable to the zonal one (Pedlosky, 1998). Circulation studies in the Subtropical Northeast Atlantic, derived from in-situ observations (Paillet and Mercier, 1997), indicate that the meridional flow is concentrated in several south-southeastwards jets. These considerations suggest that, in the study region, stretching of the weight function in zonal direction (Schmidtko et al., 2013) will not give any benefit to the final product. The topographic β-effect at the continental slope or at the MAR is several orders higher than the planetary β-effect, and cannot be neglected. Therefore, in this study, the shape of the weight function is affected by the influence of the bathymetry only.

Bathymetry data are obtained from ETOPO2 data-set (http://www.ngdc.noaa.gov/mgg/fliers/01mgg04.html), interpolated to the positions of the grid points. If the cast depth exceeds the ETOPO2 depth (typically a result of the smoothing of steep bottom slopes in ETOPO2), the first is used as the station depth. Some examples of weight distribution around a grid point in four contrasting situations are presented in Fig. 2.

Two considerations were used to obtain the radius of influence (R). First, every grid point should be obtained by averaging a sufficient amount of observations, to reduce remnant noise due to time inhomogeneity of the original data-set. A criterion of at least 30 observation points was used, suggested in statistics for obtaining a reasonable

OSD
11, 1473–1517, 2014

estimate of the first moments (Emery and Thomson, 1997). Second, R should be big enough, so that remnant traces of vortices are filtered out by the gridding procedure.

Figure 3 shows that in the upper 1900 m layer the radius of the window, containing at least 30 points, increases from 30–60 km near the Iberian Peninsula to 60–80 km in the western and southern parts of the study region. Below 1900 m, due to a drastic decrease of the number of profiles (Figs. 1d and 3c), the window radius changes across the study region from 60–150 km near the Iberian Peninsula to 150–300 km western and southern parts of the study region. On average, the radius is 40–50 km above 1900 m depth, 100 km at 2000 m and 170 km at 2400 m.

To obtain an indication of the minimum possible value of R, which is due to the remnant eddy noise, decorrelation spatial scales of temperature–salinity data were computed for each data point. Only the points which have at least 10 neighbouring observations within a 200 km radius and a 30 day period were used (Fig. 4). The decorrelation scales were estimated in 3 ways: as the point of zero crossing of a cosinusoidal fit to the autocorrelation function, as the integral of the normalized autocorrelation function from zero to the first zero-crossing, and as the integral of the square of the normalized autocorrelation function over its definition range (Stammer, 1997). The results showed that the decorrelation scales ranged from 10 to 100 km, with the mean value between 30–50 km. The histogram (Fig. 4) shows that the scales have two modes: at 10–20 km and around 30 km. The latter mode is close to the Rossby radius of deformation for the study region (Emery et al., 1984). The distribution of the decorrelation radii was rather uniform in space. It did not show any significant variations across the study region, neither with latitude, nor with the proximity to steep topography.

Values of R, a proxy for typical eddy radii, compare well with the previous studies in the region. Eddies, generated at the AzC meanders, are the main source of dynamic and temperature synoptic variability in the upper Subtropical Northeast Atlantic (Cipollini et al., 1997). For meanders, the generated eddies have the radii comparable with their quarter wavelength, which is 40–110 km (Gould, 1985; Alves and Verdière, 1999; Alves et al., 2002; Pingree, 2002). In fact, to the north of the AzC, anticyclonic

OSD
11, 1473–1517, 2014

meanders are observed to form the anticyclonic structures (Pollard and Pu, 1985; Alves and Verdière, 1999) with typical radii of 75–100 km (Pingree, 2002). To the south, the meanders form the dominating westward moving cyclones – "Storms" – with the radii of about 100 km (Pingree and Sinha, 1998; Pingree et al., 2002; Mourino et al., 2003). In the northern part of the study region, eddies are observed to have the typical radii of 10 to 50 km (Shoosmith et al., 2005). This is comparable with eddi radii of the in-situ Tourbillon experiment (around 47° N, 15° W) of 20–45 km (Arhan and Colin de Verdière, 1985; Mercier and Colin de Verdière, 1985). Near the Iberian Peninsula, water characteristics change rather drastically in space due to upwelling events, as well as the MW at mid-depths, resulting in smaller decorrelation spatial scales. In this region, the eddies have horizontal scales from 10 to 60 km (Pingree and LeCann, 1992; Oliveira et al., 2004). The characteristic eddy scales in the study region, derived from the satellite altimetry, are estimated to be 40–80 km (Le Traon et al., 1990) and 60–100 km (Stammer, 1997; Jacobs et al., 2001; Chelton et al., 2011). The overall larger radii derived from the AVISO altimetry are biased by the cut-off length-scales of 40–50 km, below which eddies cannot be detected with the gridded altimetry data. In summary, our and the previous results suggest that the eddy radii in the study region should not generally exceed 50–100 km. Therefore, to securely filter eddies in the region, the minimum R should be not less than 80–100 km. The Barnes' response function for different R is presented in Fig. 3d.

In the upper 1900 m layer, minimum R is limited by the radius of mesoscale eddies, except in the areas in the western and southwestern parts of the study region. From 2000 m level down, the scale is limited by the number of points (the requirement to have at least 30 points inside the window), and R should increase to at least twice.

To account for the decrease of the data density away from the Iberian Peninsula and, at the same time, get the highest possible resolution, two different R values were used. In the upper 1900 m layer ($G \leq 27.96\,\mathrm{kg\,m^{-3}}$), R was set to 70 km near the Iberian Peninsula and to 200 km in the open ocean. Both radii of the gridding window increased 1.5 times from approximately 1900 to 2000 m ($G = 27.97$ or $27.98\,\mathrm{kg\,m^{-3}}$) and 2 times

OSD
11, 1473–1517, 2014

below about 2000 m ($G \geq 27.99\,\mathrm{kg\,m^{-3}}$). Therefore, below 2000 m, the data-set does not permit to perform gridding with higher resolution than that of WOA13, while for the layer above an improvement can be achieved. A smooth transition between the two radii is assured. The horizontal distribution of R increases resolution towards the Iberian Peninsula (Fig. 5).

For neutral density surfaces the artificial cabelling effect due to spatial averaging was tested. These errors were so small that nudging the temperature and salinity values to return to the referred density, as applied by Schmidtko et al. (2013), was not necessary. This was a result of the small radius of averaging.

Finally, at every grid point, the vertical profiles of temperature and salinity were vertically interpolated into fixed depth levels with 25 m intervals using piecewise cubic Hermite polynomial interpolation. The cubic Hermite polynomial interpolation returns the vertical profiles differentiable to the second order without overshooting near the part of the profiles with fast changes of the function slope.

3 Results

Zonal and meridional sections of temperature and salinity obtained in this paper are presented in Fig. 6. The figure shows that over the whole study area the neutral density surfaces have a rather uniform vertical distribution. Meridional sections of temperature distribution (Fig. 6a and b) show a rapid rise of the isopycnals around 35° N (the Azores current), which is observed until the depth of 1700 m. Further north, in the upper 500 m layer, a gradual rise of the isopycnals corresponds to the dominating eastwards component of the flow. In Fig. 6a and d, one can also observe the isopycnals bending down near the MAR. This may be due to the MAR being a guide for the southward flows from the north (Bower et al., 2002).

The MW tongue extends from the Iberian Peninsula to the MAR (Fig. 6d). The saline influence of the MW extends to at least 2000 m (Reid, 1978; Harvey, 1982; Daniault et al., 1994). The colder water plume at the eastern slope of the MAR below 1500 m

OSD
11, 1473–1517, 2014

corresponds to the dominant path of the Labrador Sea Water (LSW) penetration into the eastern subtropical Atlantic (Bower et al., 2002). Further south, at 31° N (Fig. 6c), the lower fraction of the MW has the maximum near the African coast between 1000 and 1500 m. The less saline and colder core of the Antarctic Intermediate Water (AAIW) dominates the thermohaline structure further south along the African coast, at around 26–27° N (Louarn and Morin, 2011).

3.1 Comparison with WOA and MIMOC

Further on, the temperature–salinity fields obtained in this paper (MEDTRANS climatology) were compared to other existing climatologies: the WOA09, WOA13 and MIMOC data-sets (Figs. 7–9).

Figure 7 shows that temperature differences between the data-sets at 600 m do not exceed 1 °C. It is seen that the differences relative to WOA09 data-set are organized in zonally extended patterns (Fig. 7a–c). The areas of higher temperature at 600 m (Fig. 7f) correspond to the positions of the zonal jets corresponding to the branches of the NAC at 40° and 45° N (Maximenko et al., 2008). These zonal jets are seen in MIMOC, but the distribution of the characteristics in the open and coastal zones in MIMOC are also oversmoothed as compared to MEDTRANS (Fig. 7a, d, e and g). MEDTRANS climatology also shows much sharper frontal zone of the Azores current than MIMOC or WOA09 climatologies. Fewer differences are observed with WOA13. Near the Iberian Peninsula, the MEDTRANS climatology produces more details of the warmer water (upper MW core) spreading, especially along the southern coast of the Iberian Peninsula and at the Galicia Bank (Fig. 7g–i).

Figure 8 presents the salinity distribution at the depth of the lower MW core, 1200 m. The differences between the climatologies do not exceed 0.1. MEDTRANS climatology brings significantly more details on the shape of the MW tongue than WOA09 or MIMOC (Fig. 8a–g). In particular, zonally extended maximum of the MW between 30° and 33° N, from the Madeira archipelago to Cruiser-Great Meteor seamounts, is seen with higher detail. In MEDTRANS climatology exists also a weaker tongue, which

OSD
11, 1473–1517, 2014

encounters the Azores plateau from the south. MEDTRANS climatology also reproduces better the two intrusions of the Subarctic Intermediate Water (SIAW) and the Labrador Sea Water (Arhan, 1990; Bower et al., 2002): along the northeastern part of the Azores plateau (37–40° N, 24–28° W) and along the Kings rise/trough (42–45° N and 21–25° W). At the Iberian Peninsula, the important additional details of MEDTRANS climatology as compared to WOA13 are: the MUC pattern along the southern slope of the Iberian Peninsula and the MUC separation into 2 branches at the southern slope of the Galicia Bank (Fig. 8f–h).

For salinity distribution at 1700 m (Fig. 9a–c), MEDTRANS climatology again shows the MW salinity distribution with more detail as compared to WOA09, but is not intrinsically different from WOA13 (Fig. 9g–i). At the same time, MIMOC climatology shows a strange finger-like MW salinity pattern between 35° and 43° N (Fig. 9e and f). This is of artificial origin and is observed further down in MIMOC until 1900 m depth. This is not seen in the original data distributions (Fig. 1b). The salinity profiles of MIMOC climatology (Fig. 9d, profiles 3) show unrealistic deep penetration of the MW salt tongue.

Spatial distributions for a layer mean N^2 are generally similar for all the three datasets (Fig. 10). For the same latitude, the N^2 distribution represents the potential vorticity distribution and can be used for detection of water masses. The N^2 distribution in the upper main thermocline (Fig. 10a–c) displays lower values propagating from the northeastern corner, corresponding to the areas of generation and spreading of the polar fraction of the East Atlantic Central Water (Pollard et al., 1996; Paillet and Mercier, 1997). At intermediate water level (Fig. 10d–f), the N^2 minimum extending west from the Iberian Peninsula is due to the MW, and the one penetrating north along the African coast corresponds to the AAIW spreading (Louarn and Morin, 2011). At the deep water levels (Fig. 10g and h), the N^2 minimum along the eastern slope of the MAR is due to the southward spreading of the LSW (Bower et al., 2002). At those levels, MIMOC again shows deviations relative to what is expected from observations.

Figure 11 shows geostrophic currents referred to the 1900 m level, computed from the MEDTRANS, WOA13 and MIMOC climatologies. Currents from WOA09

OSD
11, 1473–1517, 2014

climatology are not presented since they are much more smoothed than even the ones from MIMOC. The reference level was chosen inside the layer where the smallest oscillations of isopycnals were observed. Figure 11a shows the currents at 100 m depth, while Fig. 11b displays the mean currents derived from AVISO altimetry (AVISO). The MEDTRANS currents are similar in structure and speed to those obtained from altimetry. This suggests that the currents at the reference level are much smaller than near the surface. MEDTRANS climatology shows the same velocities of the Azores current as in AVISO, although the flow in MEDTRANS is a bit too wide. MEDTRANS climatology also reproduces the merging of the two branches of the SNAC west of the MAR: one enters the study region at 40° N and the other at 44° N. It also shows intensifications of the flows in the northern and southern parts of the Gulf of Cadiz, as well as south of the Canary Islands. The comparison of the MEDTRANS climatology with MIMOC, clearly shows advantages of the former in detailing the representation of the circulation patterns (Fig. 11d). There are more similarities with the geostrophic currents estimated from WOA13 (Fig. 11c). Still, the latter gives less evidence of the AzC meandering and periodic intensification, also observed in AVISO maps. The WOA13 climatology does not reproduce the cyclonic gyre in the Gulf of Cadiz (Fig. 11a and b), nor the MUC outflow along the northern slope of the Gorringe and Galicia banks (Iorga and Losier, 1999) at 1000 m depth (Fig. 11e and f).

Panels a and b of Fig. 11 also reproduce the acceleration of the AzC as it turns in quasi-stationary meanders southwards, and deceleration as it turns northwards, absent in WOA13. Theory predicts such a behaviour since, in the first case, the centrifugal force is acting outwards, and in the second case, inwards (Cushman-Rosin, 2010). Therefore, in the first case, the flow acceleration increases the Coriolis force to compensate the joint acceleration due the centrifugal and pressure gradient force, while in the second case, the situation is opposite. Another feature predicted by Cushman-Rosin (2010), is that after the jets turns north in a meander, the jet deceleration results in part of the water to separate from a jet and to direct to the north, and after the jet turns south, the acceleration of the jet is accompanied by the inflow of the surrounding

OSD
11, 1473–1517, 2014

water at the north into the jet. As the jet reaches its southward point, and starts turning to the north, the initial of the jet deceleration results in another outflow from the jet, directed south. In accordance with the theory, in MEDTRANS climatology, the southward meandering of the AzC ends with the branches to the south (at 32, 28, 17 and 12° W), while northward meandering results in a northward outflow at 24° W and southward inflows as the current turns back to the south (at 20, 17 and 14° W). Therefore quasi-stationary meanders in the AzC form semiclosed water circulations to the north and to the south of the jet. Those features are also missing in WOA13 or MIMOC climatologies. Here we should point out that the symmetry of the water inflow/outflow in a meandering current, resulting from the abovementioned balance of forces, is broken due to vorticity constraint. The anticyclonic vorticity pumped into the ocean by the wind demands that the overall flow goes south (the Sverdrup balance). Therefore, the currents are more readily merging the AzC from the north and leaving from the south, than vice versa.

3.2 Seasonal variability

The gridding procedure was repeated for the warm (May to October) and the cold (November to April) seasons. The data were nearly equally distributed over the year: the cold season contained 25 000 profiles, while the warm one contained 29 000 profiles. The mean window size containing at least 30 points, increased by 30–50 %, depending on the G-level and the season. Therefore, to keep the distributions smooth enough, we increased the Barnes gridding window by 50 %: R in the upper 1900 m layer near the Iberian Peninsula was taken as 150 km, and away from that region, as 300 km.

Figure 12 presents salinity distributions during the warm and cold seasons at some water levels, as well as the respective differences. In the upper thermocline (Fig. 12a–c) the cold season is characterized by stronger meandering of the AzC between 15 and 25° W, while in summer the flows are closer to zonal. The effect is clearly seen in the seasonal variation of the geostrophic circulation patterns Fig. 13a and b, and was also

OSD
11, 1473–1517, 2014

previously observed in the AzC by Käse and Siedler (1982). More zonal extension of the flows in summer can be explained by the seasonal difference in the wind induced vorticity. In summer, the weaker winds everywhere in the study region (except for the Canary upwelling area) result in seasonal weakening of the wind stress curl by 50 % (Dee et al., 2011) and reduction of the related meridional Sverdrup transport. Therefore, Eq. (1) is better satisfied, and, in the absence of topographic slopes, currents tend to become more closely aligned with the contours of constant f than during the cold season.

Near the Iberian and African coasts, water at 200 m depth is fresher (Fig. 12c) and colder (not shown) during the warm season, when stronger southwards winds along the coast form/intensify the coastal Portugal and Canary upwellings (Navarro-Perez and Barton, 2001; Fraile-Nuez et al., 2010). This results in a stronger uplift of the isopycnals along the coasts in summer. For example, along the African coast, the summer uplift of neutral density surfaces in the upper 200 m layer is higher than in winter. The difference changes from a few meters at 34° N (Casablanca) to 25 m between 28° N (the Cape Jubi) and 33° N, and to more than 50 m at 26° N (Cape Bojador). The seasonality in the uplift quickly decreases to a few meters at 250–350 m depth between 28 and 33° N, but is observed down to 600 m at 26° N.

In the intermediate water levels, MW spreading has little seasonality (Fig. 12d–f). Still, during the warm season the MW salinity tongue at the level of the lower MW core (1000–1300 m) is more squeezed in the meridional direction and stretched further west. This may be a result of the change of the intermediate layer circulation as a delayed response to the changes in wind forcing. This mechanism was suggested as an explanation of the further penetration of AAIW along the African coast to the north of the Canary Islands during spring-summer seasons (Machin and Pelegri, 2009). The patterns of geostrophic circulation at intermediate levels are presented for the 700 m depth in Fig. 13c and d. The currents mostly show the same tendency as in the upper thermocline, the patterns being more extended in the zonal direction during summer. In particular, we note a summer intensification of the zonal flow north of the Gorringe

OSD
11, 1473–1517, 2014

Bank. Though the weak currents computed at those depths may be strongly influenced by the flows at the reference level, the pattern goes well with the extra westward penetration of MW during summer (Fig. 12d–f). At 1600 m depth, the seasonality is weak (Fig. 12g–i).

Figure 14 shows higher salinity values of the lower MW along the Iberian coast. The results show that, on average, during the warm season the MUC is more saline by 0.02–0.04, and the computed density at the maximum salinity level is larger by 0.01 kg m^{-3}. This may be the result of a more saline summer outflow from the Mediterranean Sea (Sparnocchia et al., 1994), as well as of higher salinity of the entrained NACW.

The apparent increase of the MEDTRANS gridded salinity along the southern margin of the Iberian Peninsula (Fig. 14), results from oversmoothing of the MUC characteristics during this initial phase. In fact, in this area the MUC is only 20–50 km wide (Baringer and Price, 1997) and the 70 km gridding window produces an artificial mixture of fresher and colder NACW and saltier and warmer MW. At the same time, the depth of the core should be correctly represented in the climatology. An interesting feature is that the lower MW core sudden rises at some topographically relevant locations, otherwise being quite stable. Thus, the depth of the lower core increases from 1250 to 1280 m around the Portimão canyon, then decreases by 100 m (winter) at Cape St. Vincent, Aveiro canyon, and the Cape Finisterre. These results are in accordance with compilation of the depth of the MW salinity maximum reported by several authors (e.g. Daniault et al., 1994; Bower et al., 2002).

Another feature observed in the climatology is the change of thickness of the salty MW along the Iberian continental slope. This is represented here as vertical segments in Fig. 14. On this figure, the thickness is computed between isohalines corresponding to 99 % of the maximal salinity at the section perpendicular to the isobaths (the same results are obtained using a fixed value of 36.9 for the isohaline). The thickness of the flow increases up to 38–39° N (southern flank of the Estremadura Promontory) and then starts decreasing. The MW outflow from the Straits of Gibraltar entrains 3/4 of

OSD
11, 1473–1517, 2014

the volume while passing the first 20–40 km along the northern slope of the Gulf of Cadiz at the depths of 250–500 m. Further on, entrainment into the MW continues, but to a lesser degree (Baringer and Price, 1999). The observed tendencies in the MW core thickness near the Iberian Peninsula suggest that the Estremadura Promontory is a boundary between the MUC dominated by entrainment and the MUC dominated by dissipation.

4 Conclusions

The MEDTRANS climatology is based on Barnes' optimum interpolation procedure on 53 neutral density surfaces. Due to comparatively lower along-surface gradients of temperature and salinity, as compared to the isobaric surfaces, the isoneutral gridding keeps better relative intensity of thermal and haline fronts for the same gridding radius. This was further proven when computing geostrophic current velocities in comparison with the existing high-resolution isobaric datasets (WOA09 and WOA13). The original hydrological data underwent a rigorous quality control, having passed several filtering procedures, including filtering on the neutral density surfaces. Reducing eddy related and instrumental noise, the filtering allowed sufficient smoothness of the final thermohaline fields with the enhanced spatial resolution. The gridding window radius decrease towards north-east allows using the most from the higher amount of data near the Iberian Peninsula. This leads to a better representation of thermohaline fronts of the Iberian upwelling and the MUC.

The MEDTRANS dataset can be regarded as an extension of the methodology used for obtaining MIMOC dataset (Schmidtko et al., 2013). Still there are a few important differences, which allow the MEDTRANS dataset to show several important advantages as compared to the MIMOC one. Based on vorticity considerations, topographic influence on dominant along-slope direction of water mass propagation at steep slopes, is taken into account through the shape of the gridding function. Contrary to the methodology used to produce MIMOC dataset, we limited the maximum possible extension of

OSD
11, 1473–1517, 2014

the weight function window along isobaths. This difference increases the reliability of the results along very steep slopes, where otherwise the weight function (Schmidtko et al., 2013) stretches in a very thin line with very few observational points inside the gridding window. Another difference is that the degree of extension of the gridding weights along the slope depends on the ratio of topographic to planetary β-effects. Baroclinic reduction of the topographic effect with the distance of the gridding level to the ocean bottom was also taken into account. The N/f ratio, used for definition of the maximum distance from the bottom at which the degree of topographic influence is negligible, was taken constant as it is observed in the study region. This ratio decreases towards the equatorial region and strongly increases in polar waters. In particular, in the polar regions the currents are nearly barotropic and we can assume that the bathymetry equally influences the whole water column (Cuny et al., 2002; Losch and Schröter, 2004). This change occurs in a jump when crossing the subpolar and polar fronts.

Contrary to MIMOC dataset, we did not stretch the weight function window in the zonal direction, when the influence of the bathymetry can be neglected. This is justified over most of the ocean, since the wind stress curl forces a significant meridional component of the flow. At the same time, the zonal extension may give advantages near the equator where, due to the strong meridional gradient of the Coriolis parameter, the zonal extension of the flow is well pronounced (Schmidtko et al., 2013).

The final climatological maps of temperature and salinity distribution are further vertically re-gridded to the isobaric levels to have a 25 m depth interval with around 30 km horizontal resolution.

The results suggest that the new MEDTRANS climatology, presented in this paper, gives more details on the distribution of water characteristics, in the upper 2000 m layer of the Subtropical Northeast Atlantic, than other databases. The geostrophic currents in the upper layer revealed several features, not reproduced by the existing climatologies, but all in close correspondence with theory (Cushman-Rosin, 2010) and with independent observations (e.g. Lozier et al., 1995; New et al., 2001): (i) periodic

OSD
11, 1473–1517, 2014

intensification of the AzC as it turns south in the quasistationary meanders; (ii) inflows and outflows from the AzC as it meanders; (iii) recirculation of the AzC west of Cruiser-Great Meteor seamounts; (iv) cyclonic beta-gyre in the Gulf of Cadiz. At 1000 m depth, the geostrophic currents referred to 1900 m level, derived from the MEDTRANS dataset, show two veins of the MUC along the western slope of the Iberian Peninsula: one travels along the slope, while the other separates from the slope around the Gorringe Bank and then flows north and merges with the other vein, south of the Galicia Bank. Here the MUC splits again into a vein along the continental slope to the north and along the southwestern slope of the Galicia Bank to the northeast. The currents were obtained from an independent dataset (Iorga and Losier, 1999) but do not appear in WOA13 climatology.

The seasonality of the MW water manifested itself in stronger zonal extension of the flows during the warm season. This may be related with the decrease of the wind stress curl, and the related Sverdrup fluxes, in the northern and central parts of the study region. The seasonality in the MW manifested itself in more saline and denser MW lower core in the MUC during the warm season. Also stronger seawards extension of the MW salt tongue is observed in summer. The thermohaline observations are confirmed by the geostrophic currents at 1000 m referred to 1900 m level, as derived from the MEDTRANS data-set. The MW outflow does not appear at other climatologies, including WOA13.

The gridded fields are available at the web-site of the Center of Oceanography of the University of Lisbon (http://co.fc.ul.pt/pt/2014-02-05-11-58-42).

Acknowledgements. The authors acknowledge the scientific project MEDTRANS (PTDC/MAR/117265/2010), sponsored by the Portuguese Foundation for Science and Technology (FCT) and the Center of Oceanography of the University of Lisbon. I.B. also acknowledges the contract C2008-UL-CO-3 of Ciência 2008 between Foundation for Science and Technology (FCT) and the University of Lisbon (UL).

OSD
11, 1473–1517, 2014

References

Alves, M. L. G. R. and de Verdière, A. C.: Instability dynamics of a subtropical jet and applications to the Azores current system: eddy-driven mean flow, J. Phys. Oceanogr., 29, 837–864, 1999.

Alves, M. L. G. R., Gaillard, F., Sparrow, M., Knoll, M., and Giraud, S.: Circulation patterns and transport of the Azores front-current system, Deep-Sea Res. Pt. II, 49, 3983–4002, 2002.

Ambar, I.: A shallow core of Mediterranean water off western Portugal, Deep-Sea Res. Pt. I, 30, 677–680, 1983.

Ambar, I., Serra, N., Neves, F., and Ferreira, T.: Observations of the Mediterranean Undercurrent and eddies in the Gulf of Cadiz during 2001, J. Marine Syst., 71, 195–220, 2008.

Arhan, M.: The North Atlantic Current and Subarctic Intermediate Water, J. Mar. Res., 48, 109–144, 1990.

Arhan, M. and Colin de Verdière, A.: Dynamics of eddy motions in the eastern North Atlantic, J. Phys. Oceanogr., 15, 153–170, 1985.

AVISO data set: The altimeter products were produced by Ssalto/Duacs and distributed by Aviso, with support from Cnes, available at: http://las.aviso.oceanobs.com/las/getUI.do (last access: 9 June 2014), 2014.

Baringer, M. N. and Price, J. F.: Mixing and spreading of the Mediterranean outflow, J. Phys. Oceanogr., 27, 1654–1677, 1997.

Baringer, M. N. and Price, J. F.: A review of the physical oceanography of the Mediterranean outflow, Mar. Geol., 155, 63–82, 1999.

Barnes, S. L.: A technique for maximizing details in numerical weather map analysis, J. Appl. Meteorol., 3, 396–409, 1964.

Bower, A. S., Le Cann, H., Rossby, T., Zenk, W., Gould, J., Speer, K., Richardson, P. L., Prater, M. D., and Zhang, H. M.: Directly measured mid-depth circulation in the North Atlantic Ocean, Nature, 419, 603–607, 2002.

Chelton, D. B., Schlax, M. G., and Samelson, R. M.: Global observations of nonlinear mesoscale eddies, Prog. Oceanogr., 91, 167–216, 2011.

Cipollini, P., Cromwell, D., Jones, M. S., Quartly, G. D., and Challenor, P. G.: Concurrent altimeter and infrared observations of Rossby wave propagation near 34° N in the Northeast Atlantic, Geophys. Res. Lett., 24, 889–892, 1997.

OSD
11, 1473–1517, 2014

Comas-Rodríguez, I., Hernández-Guerra, A., Fraile-Nuez, E., Martínez-Marrero, A., Benítez-Barrios, V. M., Pérez-Hernández, M. D., and Vélez-Belchí, P.: The Azores Current System from a meridional section at 24.5° W, J. Geophys. Res., 116, C09021, doi:10.1029/2011JC007129, 2011.

Cuny, J., Rhines, P. B., Niiler, P. P., and Bacon, S.: Labrador Sea boundary currents and the fate of the Irminger Sea Water, J. Phys. Oceanogr., 32, 627–647, 2002.

Cushman-Roisin, B.: Environmental Fluid Mechanics, John Wiley & Sons, NY, 400 pp., 2010.

Daniault, N., Mazé, J. P., and Arhan, M.: Circulation and mixing of Mediterranean Water west of the Iberian Peninsula, Deep-Sea Res. Pt. I, 41, 1685–1714, 1994.

Dee, D. P., Uppala, S. M., Simmons, A. J., Berrisford, P., Poli, P., Kobayashi, S., Andrae, U., Balmaseda, M. A., Balsamo, G., Bauer, P., Bechtold, P., Beljaars, A. C. M., van de Berg, L., Bidlot, J., Bormann, N., Delsol, C., Dragani, R., Fuentes, M., Geer, A. J., Haimberger, L., Healy, S. B., Hersbach, H., Hólm, E. V., Isaksen, L., Kållberg, P., Köhler, M., Matricardi, M., McNally, A. P., Monge-Sanz, B. M., Morcrette, J. J., Park, B. K., Peubey, C., de Rosnay, P., Tavolato, C., Thépaut, J. N., and Vitart, F.: The ERA-Interim reanalysis: configuration and performance of the data assimilation system, Q. J. Roy. Meteor. Soc., 137, 553–597, doi:10.1002/qj.828, 2011.

Emery, W. J. and Thomson, R. E.: Data Analysis Methods in Physical Oceanography, Pergamon, UK, 1–634, 1997.

Emery, W. J., Lee, W. G., and Magaard, L.: Geographic and seasonal distributions of Brunt–Väisälä frequency and Rossby radii in the North Pacific and North Atlantic, J. Phys. Oceanogr., 14, 294–317, 1984.

Fraile-Nuez, E., Machín F., Vélez-Belchí P., López-Laatzen, F., Borges, R., Benítez-Barrios, V., and Hernández-Guerra, A.: Nine years of mass transport data in the eastern boundary of the North Atlantic Subtropical Gyre, J. Geophys. Res., 115, C09009, doi:10.1029/2010JC006161, 2010.

Gould, W. J.: Physical oceanography of the Azores front, Prog. Oceanogr., 14, 167–190, 1985.

Harvey, J.: θ–S relationships and water masses in the eastern North Atlantic, Deep-Sea Res., 29, 1021–1033, 1982.

Iorga, M. C. and Lozier, M. S.: Signature of the Mediterranean outflow from a North Atlantic climatology: 1. Salinity and density fields, J. Geophys. Res., 104, 25985–26009, 1999.

Jacobs, G. A., Barron, C. N., and Rhodes, R. C.: Mesoscale characteristics, J. Geophys. Res., 106, 19581–19595, 2001.

OSD
11, 1473–1517, 2014

Jackett, D. R. and McDougall, T. J.: A Neutral Density Variable for the World's Oceans, J. Phys. Oceanogr., 27, 237–263, 1997.
Jia, Y.: Formation of an Azores Current due to Mediterranean overflow in a modeling study of the North Atlantic, J. Phys. Oceanogr., 30, 2342–2358, 2000.
Käse, R. H. and Siedler, G.: Meandering of the subtropical front south-east of the Azores, Nature, 300, 245–246, 1982.
Klein, B. and Siedler, G.: On the origin of the Azores current, J. Geophys. Res., 94, 6159–6168, 1989.
Le Traon, P. Y., Rouquet, M. C., and Boissier, C.: Spatial scales of mesoscale variability in the North Atlantic as deduced from Geosat data, J. Geophys. Res., 95, 20267–20285, 1990.
Levitus, S., Antonov, J., and Boyer, T.: Global ocean heat content 1955–2007 in light of recently revealed instrumentation problems, Geophys. Res. Lett., 36, L07608, doi:10.1029/2008GL037155, 2008.
Losch, M. and Schröter, J.: Estimating the circulation from hydrography and satellite altimetry in the Southern Ocean: limitations imposed by the current geoid models, Deep-Sea Res. Pt. I, 51, 1131–1143, 2004.
Louarn, E. and Morin, P.: Antarctic Intermediate Water influence on Mediterranean Sea water outflow, Deep-Sea Res. Pt. I, 58, 932–942, 2011.
Lozier, M. S., McCartney, M. S., and Owens, W. B.: Anomalous anomalies in averaged hydrographic data, J. Phys. Oceanogr., 24, 2624–2638, 1994.
Lozier, M. S., Owens, W. B., and Curry, R. G.: The climatology of the North Atlantic, Prog. Oceanogr., 36, 1–44, 1995.
Machín, F. and Pelegrí, J. L.: Northward penetration of Antarctic intermediate water off Northwest Africa, J. Phys. Oceanogr., 39, 512–535, 2009.
Martins, C. S., Hamann, M., and Fuiza, A. F. G.: Surface circulation in the eastern North Atlantic from drifters and altimetry, J. Geophys. Res., 107, 3217, doi:10.1029/2000JC000345, 2002.
Maximenko, N. A., Melnichenko, O. V., Niiler, P. P., and Sasaki, H.: Stationary mesoscale jet-like features in the ocean, Geophys. Res. Lett., 35, L08603, doi:10.1029/2008GL033267, 2008.
McDougall, T. J.: Neutral density surfaces, J. Phys. Oceanogr., 17, 1950–1964, 1987.
Melet, A., Nikurashin, M., Muller, C., Falahat, S., Nycander, J., Timko, P. G., Arbic, B. K., and Goff., J. A.: Internal tide generation by abyssal hills using analytical theory, J. Geophys. Res.-Oceans, 118, 6303–6318, doi:10.1002/2013JC009212, 2013.

OSD
11, 1473–1517, 2014

Mercier, H. and Colin de Verdière, A.: Space and time scales of mesoscale motions in the eastern North Atlantic, J. Phys. Oceanogr., 15, 171–183, 1985.
Mourino, B., Fernandez, E., Etienne, H., Hernandez, F., and Giraud, S.: Significance of cyclonic SubTropical Oceanic Rings of Magnitude (STORM) eddies for the carbon budget of the euphotic layer in the subtropical northeast Atlantic, J. Geophys. Res., 108, 3383, doi:10.1029/2003JC001884, 2003.
Navarro-Pérez, E. and Barton, E. D.: Seasonal and interannual variability of the Canary Current, Sci. Mar., 65, 205–213, 2001.
New, A. L., Jia, Y., Coulibaly, M., and Dengg, J.: On the role of the Azores current in the ventelation of the North Atlantic Ocean, Prog. Oceanogr., 48, 163–194, 2001.
Nolasco, R., Cordeiro Pires, A., Cordeiro, N., and Dubert, J.: A high-resolution modeling study of the Western Iberian Margin mean and seasonal upper ocean circulation, Ocean Dynam., 63, 1041–1062, 2013.
Oliveira, P. B., Peliz, A., Dubert, J., Rosa, T. L., and Santos, A. M. P.: Winter geostrophic currents and eddies in the western Iberia coastal transition zone, Deep-Sea Res. Pt. I, 51, 367–381, 2004.
Onken, R.: The Azores Countercurrent, J. Phys. Oceanogr., 23, 1638–1646, 1993.
Owens, W. B. and Hogg, N. G.: Oceanic observations of stratified Taylor columns near a bump, Deep-Sea Res., 27, 1029–1045, 1980.
Paillet, J. and Mercier, H.: An inverse model of the eastern North Atlantic general circulation and thermocline ventilation, Deep-Sea Res. Pt. I, 44, 1293–1328, 1997.
Pedlosky, J.: Ocean Circulation Theory, 2nd edn., Springer, New York, 1–453, 1998.
Pelegri, J. L., Arístegui, J., Cana, L., González-Dávila, M., Hernández-Guerra, A., Hernández-León, S., Marrero-Díaz, A., Montero, M. F., Sangrà, P., and Santana-Casiano, M.: Coupling between the open ocean and the coastal upwelling region off northwest Africa: water recirculation and offshore pumping of organic matter, J. Marine Syst., 54, 3–37, 2005.
Perez, F. F., Mintrop, L., Llinas, O., Glez-Davila, M., Castro, C. G., Alvarez, M., and Kortzinger, A.: Mixing analysis of nutrients, oxygen and inorganic carbon in the Canary Islands region, J. Marine Syst., 28, 183–201, 2001.
Pingree, R. D.: Ocean structure and climate (Eastern North Atlantic): in situ measurement and remote sensing (altimeter), J. Mar. Biol. Assoc. UK, 82, 681–707, 2002.
Pingree, R. D. and Le Cann, B.: Anticyclonic eddy X91 in the southern Bay of Biscay, May 1991 to February 1992, J. Geophys. Res., 97, 14353–14367, 1992.

OSD
11, 1473–1517, 2014

Pingree, R. D. and Sinha, B.: Dynamic topography (ERS-1/2 and sea truth) of subtropical ring (STORM 0 in the STORM Corridor (32–34° N), Eastern Basin, North Atlantic Ocean, J. Mar. Biol. Assoc. UK, 78, 351–376, 1998.
Pingree, R. D., Kou, Y. H., and Garcia-Soto, C.: Can Subtropical North Atlantic permanent thermocline be observed from space?, J. Mar. Biol. Assoc. UK, 82, 709–728, 2002.
Pollard, R. T. and Pu, S.: Structure and circulation of the upper Atlantic ocean northeast of the Azores, Prog. Oceanogr., 14, 443–462, 1985.
Pollard, R. T., Griffiths, M. J., Cunningham, S. A., Read, J. F., Perez, F. F., and Rios, A. F.: Vivaldi 1991 – a study of the formation, circulation and ventilation of Eastern North Atlantic Central Water, Prog. Oceanogr., 37, 167–192, 1996.
Reid, J. L.: On the middepth circulation and salinity field in the North Atlantic Ocean, J. Geophys. Res., 83, 5063–5067, doi:10.1029/JC083iC10p05063, 1978.
Richardson, P. L., McCartney, P. L., and Maillard, C.: A search for Meddies in historical data, J. Phys. Oceanogr., 15, 241–265, 1991.
Roemmich, D. and Gilson, J.: The 2004–2008 mean and annual cycle of temperature, salinity, and steric height in the global ocean from the Argo Program, Prog. Oceanogr., 82, 81–100, 2009.
Schmidtko, S., Johnson, G. C., and Lyman, J. M.: MIMOC: a global monthly isopycnal upper-ocean climatology with mixed layers, J. Geophys. Res.-Oceans, 118, 1658–1672, 2013.
Shoosmith, D. R., Richardson, P. L., Bower, A. S., and Rossby, H. T.: Discrete eddies in the northern North Atlantic as observed by looping RAFOS floats, Deep-Sea Res. Pt. II, 52, 627–650, 2005.
Sparnocchia, S., Manzella, G. M., and La Violette, P. E.: The interannual and seasonal variability of the MAW and LIW core properties in the Western Mediterranean Sea, Coast. Estuar. Stud., 46, 177–194, 1994.
Stammer, D.: Global characteristics of ocean variability estimated from regional TOPEX/POSEIDON altimeter measurements, J. Phys. Oceanogr., 27, 1743–1769, 1997.
Troupin, C., Machín, F., Ouberdous, M., Sirjacobs, D., Barth, A., and Beckers, J. M.: High-resolution climatology of the northeast Atlantic using Data-Interpolating Variational Analysis (Diva), J. Geophys. Res., 115, C08005, doi:10.1029/2009JC005512, 2010.
Volkov, D. L. and Fu, L. L.: On the reasons for the formation and variability of the Azores Current, J. Phys. Oceanogr., 40, 2197–2220, 2010.

OSD
11, 1473–1517, 2014

WOA09: World Ocean Atlas 2009, vol. 1: Temperature, edited by: Levitus, S., NOAA Atlas NESDIS 68, US Government Printing Office, Washington DC, 184 pp., temperature compiled by: Locarnini, R. A., Mishonov, A. V., Antonov, J. I., Boyer, T. P., Garcia, H. E., Baranova, O. K., Zweng, M. M., and Johnson, D. R., vol. 2: Salinity, edited by: Levitus, S., NOAA Atlas NESDIS 69, US Government Printing Office, Washington DC, 184 pp., salinity compiled by: Antonov, J. I., Seidov, D., Boyer, T. P., Locarnini, R. A., Mishonov, A. V., Garcia, H. E., Baranova, O. K., Zweng, M. M., and Johnson, D. R., available at: http://www.nodc.noaa.gov/OC5/WOA09/pubwoa09.html (last access: 5 June 2014), 2009.

WOA13: World Ocean Atlas 2013, vol. 1: Temperature, edited by: Levitus, S. and Mishonov, A., NOAA Atlas NESDIS 73, 40 pp., temperature compiled by: Locarnini, R. A., Mishonov, A. V., Antonov, J. I., Boyer, T. P., Garcia, H. E., Baranova, O. K., Zweng, M. M., Paver, C. R., Reagan, J. R., Johnson, D. R., Hamilton, M., and Seidov, D., vol. 2: Salinity, edited by: Levitus, S. and Mishonov, A., NOAA Atlas NESDIS 74, 39 pp., salinity compiled by: Zweng, M. M., Reagan, J. R., Antonov, J. I., Locarnini, R. A., Mishonov, A. V., Boyer, T. P., Garcia, H. E., Baranova, O. K., Johnson, D. R., Seidov, D., and Biddle, M. M., available at: http://www.nodc.noaa.gov/OC5/ (last access: 5 June 2014), 2013.

WOD: World Ocean Database 2013, edited by: Levitus, S. and Mishonov, A., NOAA Atlas NESDIS 72, 209, 2013.

OSD
11, 1473–1517, 2014

Table 1. Profiles statistics per instrument type.

data type	number of profiles	> 50 % good in temperature and salinity
CTD	9973	99 %
PFL	21 634	96 %
OSD	22 822	90 %
Total	54 429	94 %

OSD
11, 1473–1517, 2014

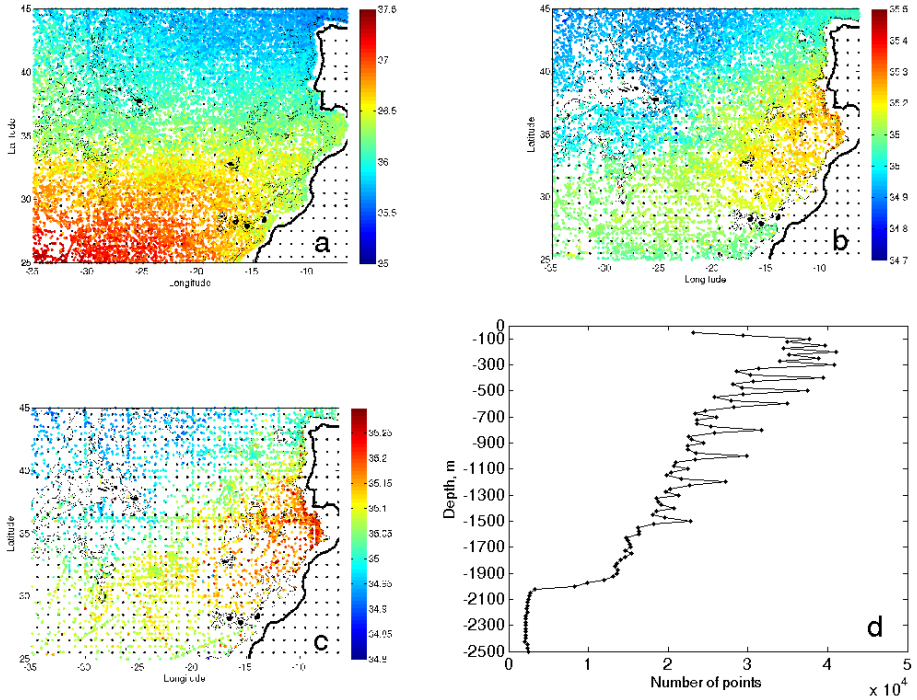

Figure 1. Scatter plot of valid salinity data-points **(a)** at 100 m, **(b)** 1900 m, **(c)** 2000 m and **(d)** the vertical profile of the total number of valid salinity data points. WOA09 grid is shown on **(a–c)** with black dots. The colour scale represents salinity.

OSD
11, 1473–1517, 2014

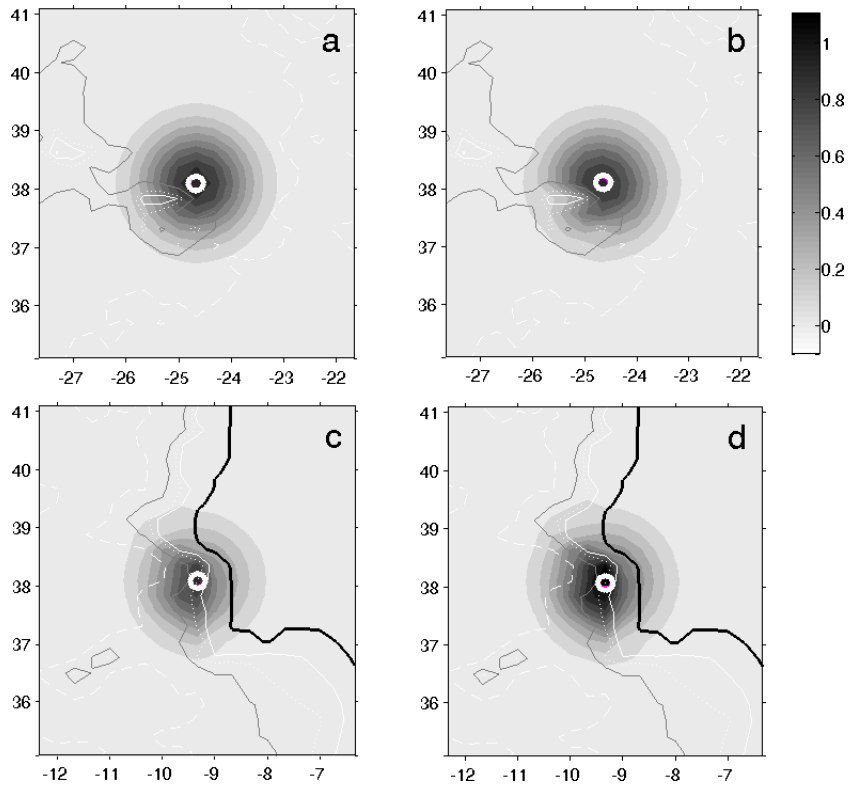

Figure 2. Weight function (W) **(a)** for small effect of topography at 100 m, **(b)** stronger effect at the same location at 1500 m and **(c–d)** the dominating effect of topography near the continental slope at 100 m. Lower panels show the shape of the weight function **(c)** when the correction factor w is not applied, and **(d)** with the correction factor w applied. The color scale marks the distribution of the weights as a function of the distance from the central grid-point (marked with the white ring). Topographic contours of 0, 500, 1000, 2000, 3000 and 4000 m are presented for reference.

OSD
11, 1473–1517, 2014

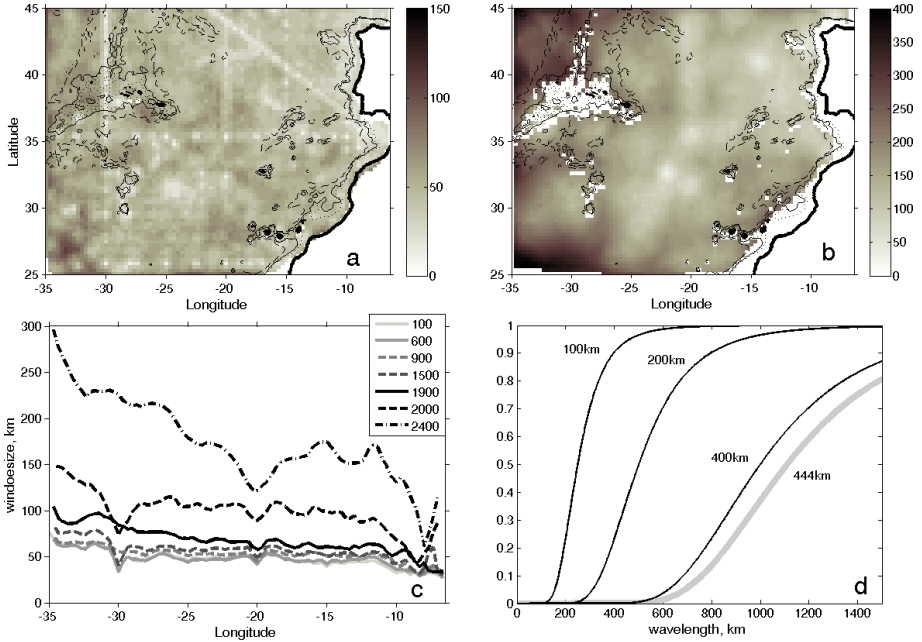

Figure 3. Radius (km) of the window containing a minimum of 30 data points: **(a)** at 100 m and **(b)** at 2500 m depth. **(c)** Variation of the window size as a function of the distance from the coast and water level. **(d)** Barnes' response function for different radii of averaging after the 3rd iteration.

OSD
11, 1473–1517, 2014

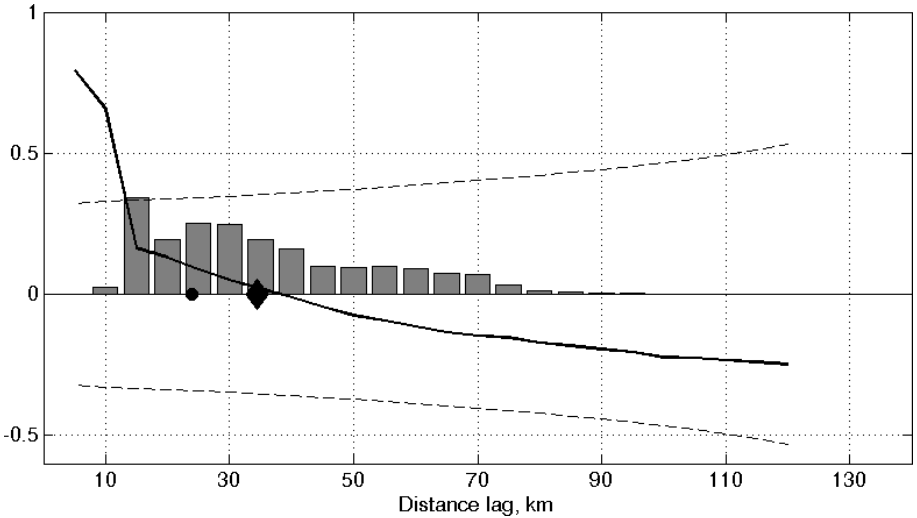

Figure 4. Decorrelation scales (radii): black curve is the mean autocorrelation function, black diamond is the mean of the decorrelation scales, while black disk is the decorrelation scale computed from the mean autocorrelation function (black curve). Dash lines mark the level of significance of the mean autocorrelation function.

OSD
11, 1473–1517, 2014

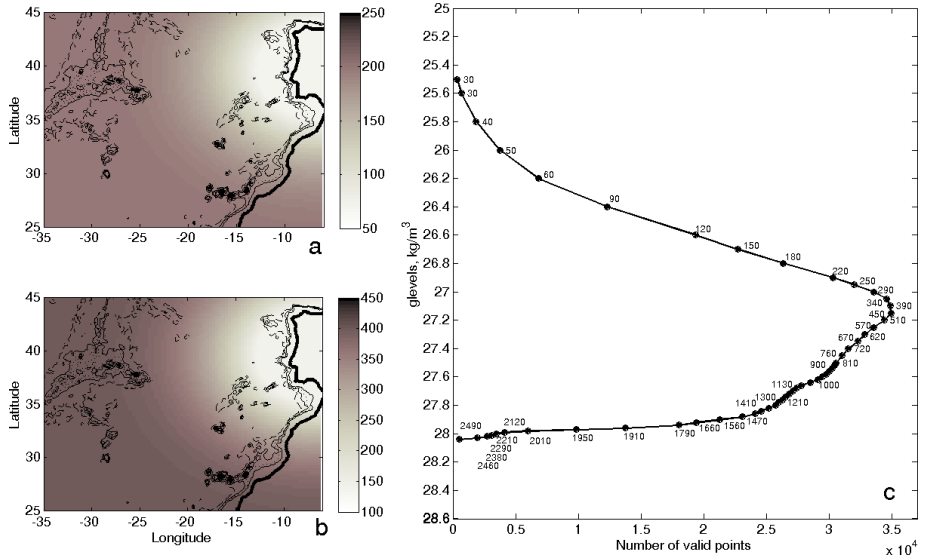

Figure 5. Spatial variation of R in **(a)** the upper 1900 m layer; **(b)** below 2000 m. **(c)** presents total number of valid salinity data points at the selected neutral density surfaces. The numbers to the right of the black filled circles mark area-mean depth of the neutral density surface in the study region (not all numbers are presented).

OSD
11, 1473–1517, 2014

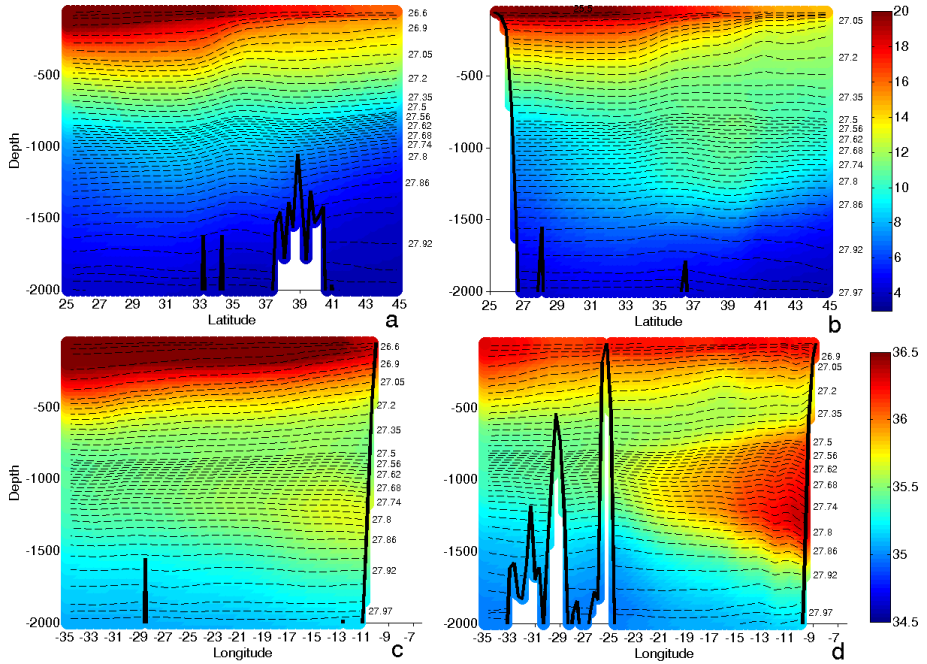

Figure 6. Vertical meridional sections of temperature along **(a)** 30° W and **(b)** 15° W; and zonal sections of salinity along **(c)** 31° N and **(d)** 38° N. The dashed isolines show positions of neutral density surfaces (only part of the surfaces used are shown).

OSD
11, 1473–1517, 2014

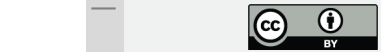

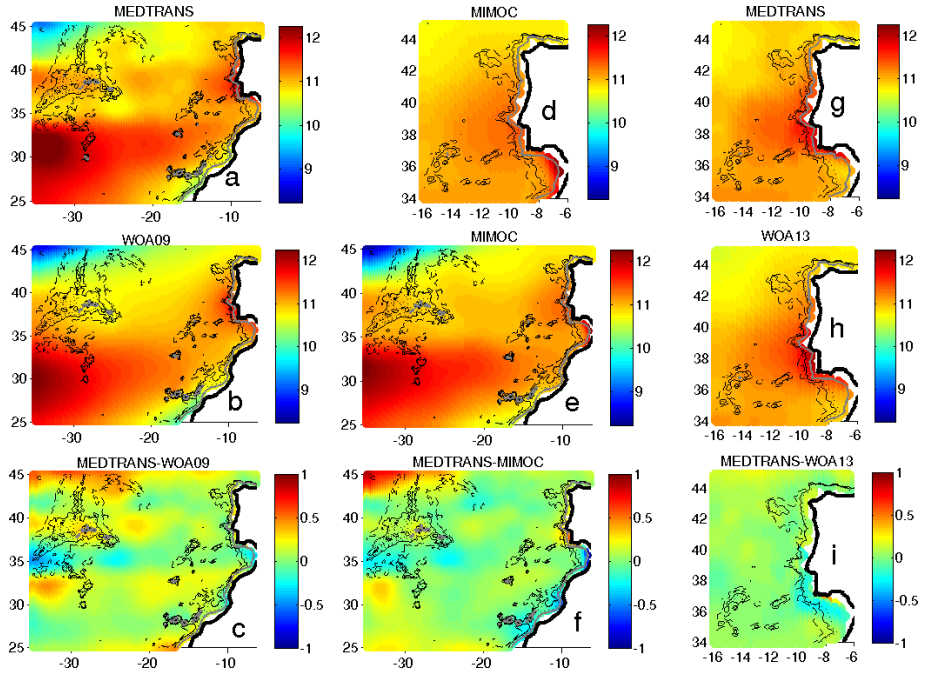

Figure 7. Temperature at 600 m. (**a** and **g**) – MEDTRANS, **(b)** – WOA09, **(c)** – MEDTRANS minus WOA09, (**d** and **e**) – MIMOC, **(f)** – MEDTRANS minus MIMOC, **(h)** – WOA13, **(i)** – MEDTRANS minus WOA13.

OSD
11, 1473–1517, 2014

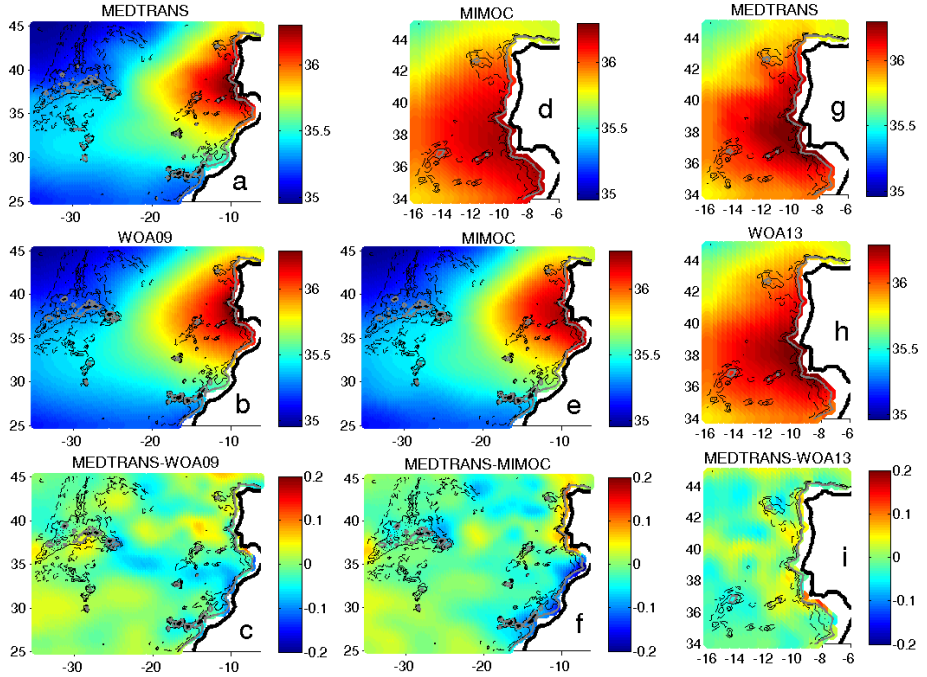

Figure 8. Salinity at 1200 m. (**a** and **g**) – MEDTRANS, **(b)** – WOA09, **(c)** – MEDTRANS minus WOA09, (**d** and **e**) – MIMOC, **(f)** – MEDTRANS minus MIMOC, **(h)** – WOA13, **(i)** – MEDTRANS minus WOA13.

OSD
11, 1473–1517, 2014

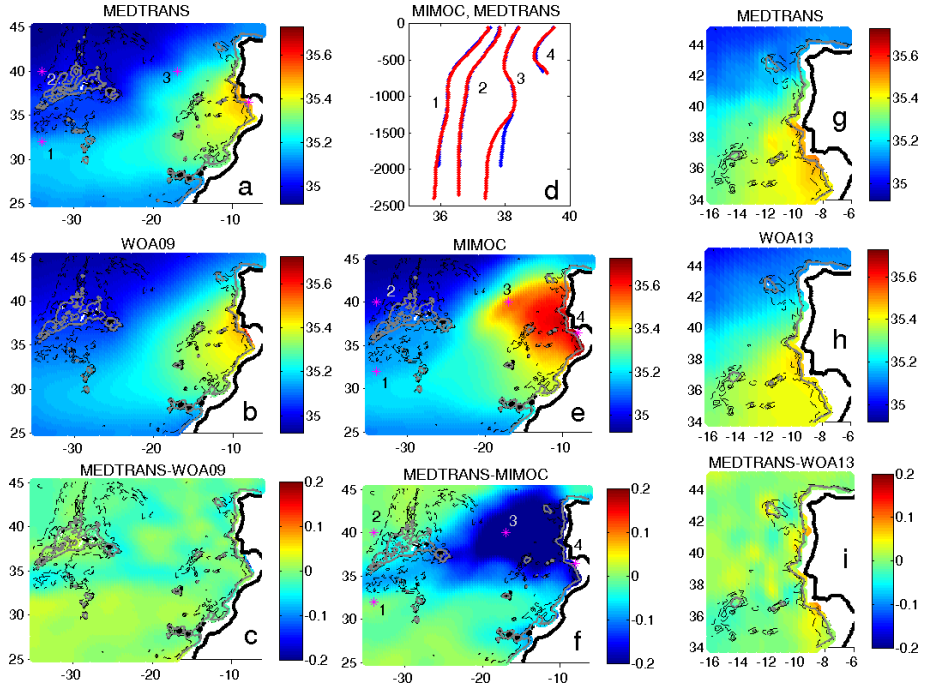

Figure 9. Salinity at 1700 m. (**a** and **g**) – MEDTRANS, **(b)** – WOA09, **(c)** – MEDTRANS minus WOA09, **(e)** – MIMOC, **(f)** – MEDTRANS minus MIMOC, **(h)** – WOA13, **(i)** – MEDTRANS minus WOA13. In panel **(d)** are presented vertical profiles of MEDTRANS (red) and MIMOC (blue) at the points: 1 (32° N, 34° W), 2 (40° N, 34° W), 3 (40° N, 17° W), 4 (37° N, 8° W).

OSD
11, 1473–1517, 2014

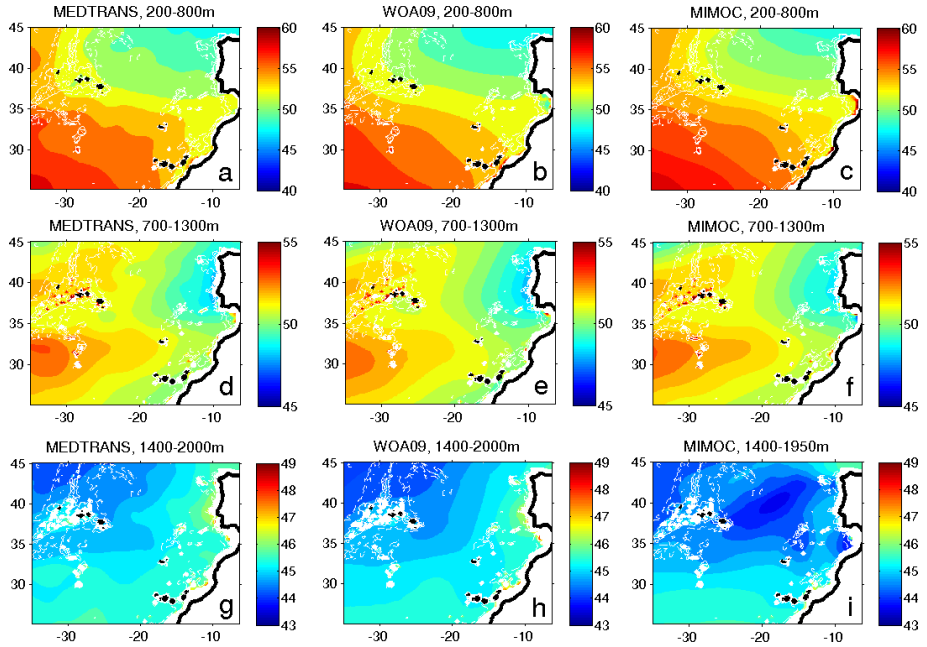

Figure 10. N^2 mean **(a–c)** from 200 to 800 m, **(d–f)** from 700 to 1300 m, and **(g–i)** from 1400–2000 m, for MEDTRANS (the first column), WOA09 (the second column) and MIMOC (the third column).

OSD
11, 1473–1517, 2014

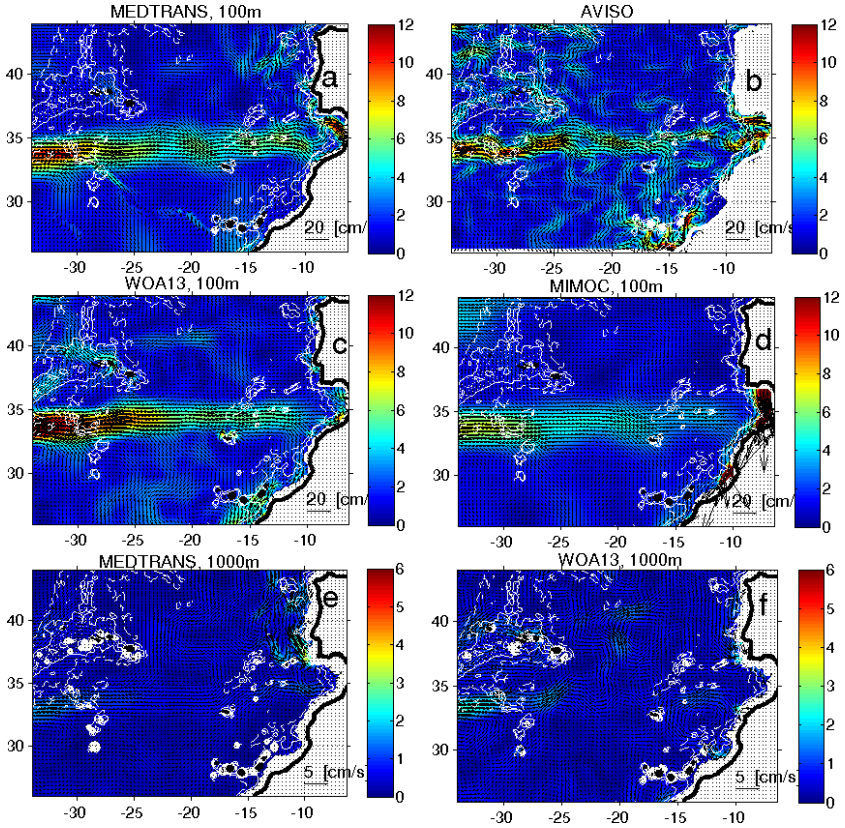

Figure 11. Velocity of geostrophic currents (cm s^{-1}) at 100 m referenced to 1900 m, derived from **(a)** MEDTRANS, **(c)** WOA13 and **(d)** MIMOC climatologies. AVISO surface currents, averaged between 1992 and 2012, are presented in **(b)**. Velocity of geostrophic currents at 1000 m referenced to 1900 m (cm s^{-1}), derived from **(e)** MEDTRANS climatology and **(f)** WOA13. For reference, 2000 m and 3000 m depth contours are shown in white.

OSD
11, 1473–1517, 2014

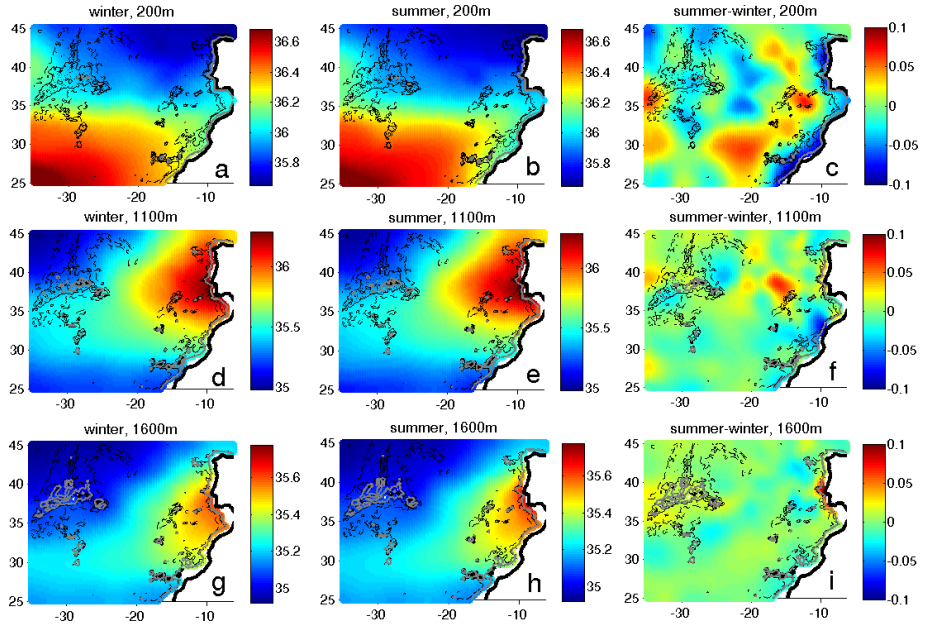

Figure 12. Salinity at **(a–b)** 200 m, **(d–e)** 1100 m and **(g–h)** 1600 m: **(a)**, **(d)** and **(g)** – winter; **(b)**, **(e)** and **(h)** – summer; **(c)**, **(f)** and **(i)** – difference between summer and winter climatologies.

OSD
11, 1473–1517, 2014

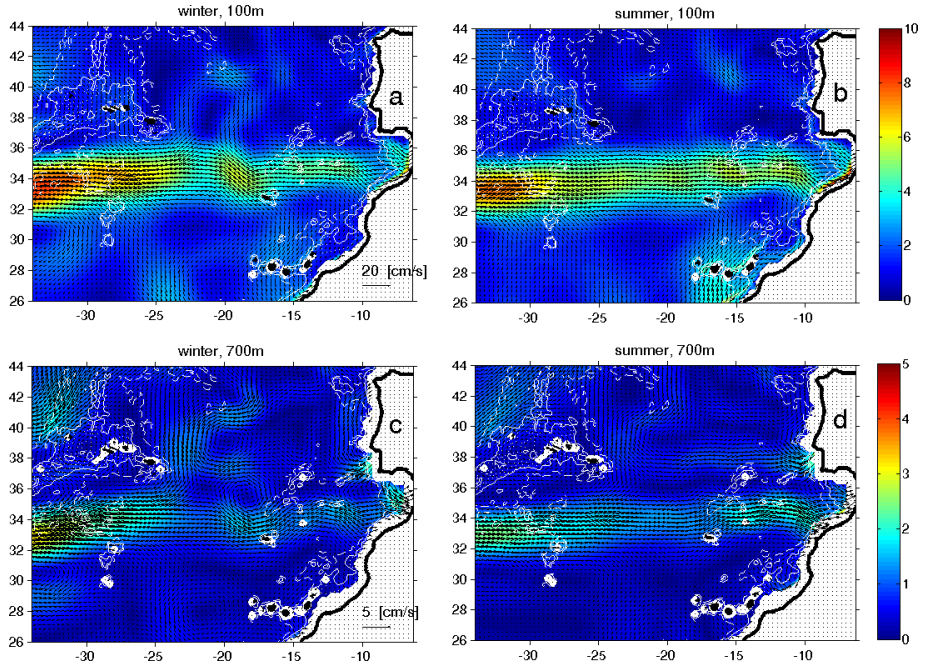

Figure 13. Velocity of geostrophic currents (cm s^{-1}) at 100 m and 700 m levels, referenced to 1900 m: **(a)** 100 m winter, **(b)** 100 m summer, **(c)** 700 m winter, **(d)** 700 m summer.

OSD
11, 1473–1517, 2014

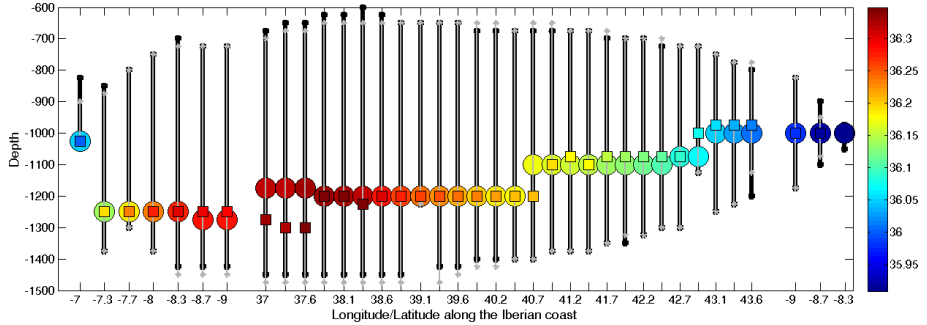

Figure 14. Seasonal variations of the depth and salinity of the MW lower core along the Iberian slope in winter (disks) and summer (squares). The vertical segments represent the maximum depth limits of $S \geq 0.99 \cdot S_{max}$ at the section.

OSD
11, 1473–1517, 2014